Geophysical Research Letters

Supporting Information for

Observing posteruptive deflation of hydrothermal system using InSAR time series analysis: An application of ALOS-2/PALSAR-2 data on the 2015 phreatic eruption of Hakone volcano, Japan

by R. Doke[1], K. Mannen[1], and K. Itadera[1]

[1] Hot Springs Research Institute of Kanagawa Prefecture, 586 Iriuda, Odawara, Kanagawa 250-0031, Japan.

Contents of this file

Introduction

Test S1 describes the methods and results of model inversion. Figure S1 shows the temporal and spatial baselines for the SBAS-InSAR time series analysis of ALOS-2/PALSAR-2 data. Figures S2 and S3 show the results of the model inversion. Figures S4 and S5 show the standard deviations of and tradeoffs among the model parameters for the point source and sill deflation models, respectively. Table S1 gives the ALOS-2/PALSAR-2 data used in this study.

Text S1. Model Inversion

Model inversion was performed to explain the surface velocity distributions obtained from the SBAS-InSAR time series analysis. Before the modeling, the surface velocity maps (Figure 2) were subsampled using the quadtree-partitioning algorithm (Jonsson, 2002; Welstead, 1999) to reduce the influence of noise. In the algorithm, a scene is divided into four quadrants, and the root mean square (RMS) of the surface velocity for each quadrant was calculated. If the RMS of the quadrant exceeds a given threshold, the quadrant is divided into four new quadrants, and the RMS of each is calculated and again compared with the threshold. The subdividing process was continued until the RMS of the surface velocity dropped below the threshold or a given maximum number of subdivision steps was reached. In this study, the RMS threshold was set to 1 mm/yr, and the maximum number of steps was set to 6. Because the size of the smallest quadrant (a mesh of approximately 300 m in the E–W direction) is comparable to or slightly larger than the observed significant local displacements, such as the landslide in Owakudani, such observations can be expected to produce no significant effect on this model evaluation, which focuses on large-scale displacements. The subsampled datasets consist of 346 and 339 points for paths 126 and 18, respectively (Figures S2(a), (b) and S3 (a), (b)).

Here, we employed two deflation source models: a point pressure source model (Mogi, 1958) and a rectangular sill model (tensile fault model by Okada, 1985) in a semi-infinite elastic crust. To consider the effect of topography, the elevations of observed points in datasets were compensated. The optimal parameters of the models were estimated using a modeling tool in ENVI SARscape, which employs the nonlinear inversion algorithm based on the Levenberg–Marquardt least-squares approach (Marquardt, 1963). The offsets of the datasets were also estimated assuming a linear ramp, along with the parameters of the model. After the best-fit parameters were obtained, the standard deviations of each parameter were determined from the results of another 250 iterations. The standard errors were calculated as the standard deviations divided by the square root of the number of iterations. Additionally, the tradeoff relationships among the parameters were visualized based on the iteration results (Figures S4 and S5).

Figures S2 and S3 show the surface velocities simulated by the optimal point source and sill deflation models, respectively. The optimal parameters estimated from the model inversion are given in Table 1 with their standard errors.

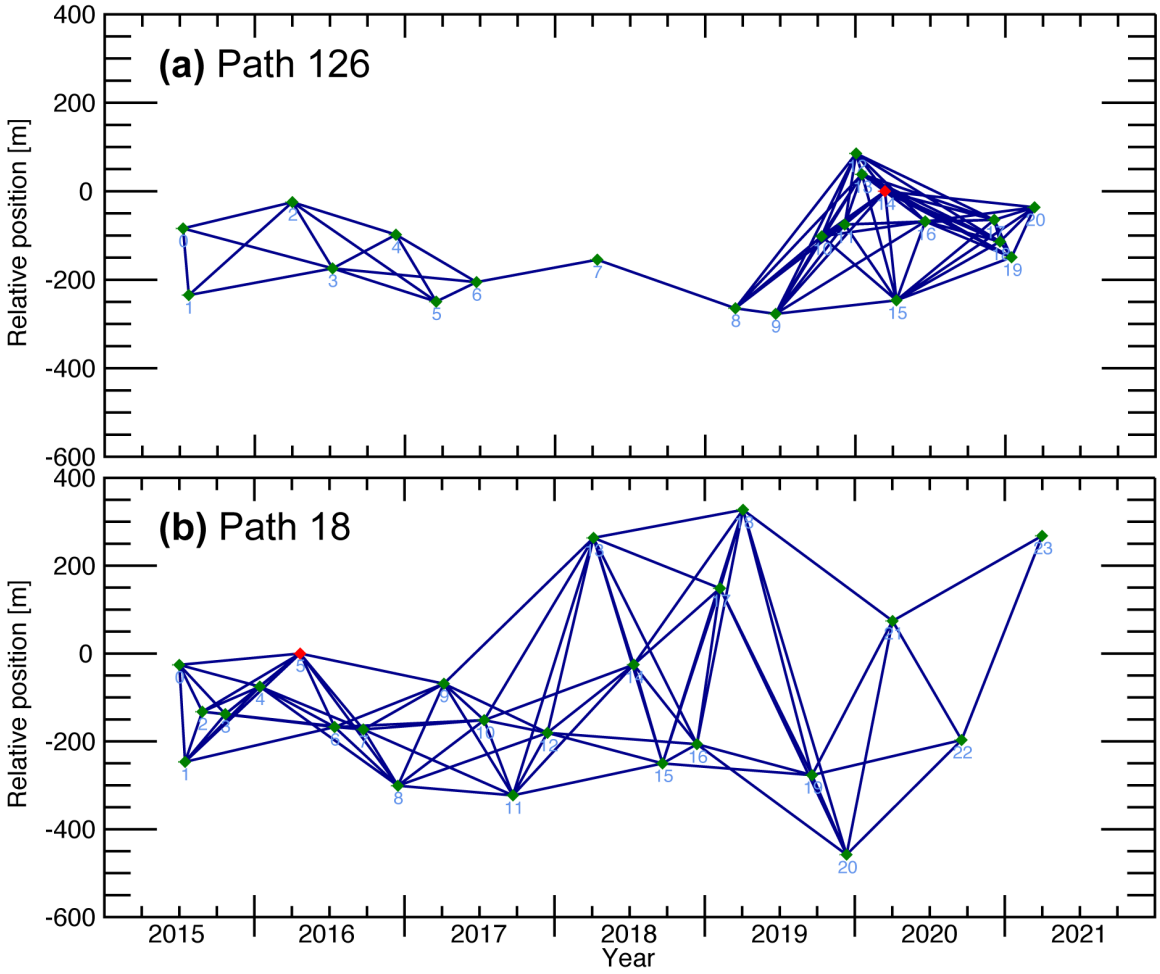

Figure S1. Temporal and spatial baselines for the SBAS-InSAR time series analysis of ALOS-2/PALSAR-2 data from (a) path 126 and (b) path 18. Red points show the super primary scenes used for the analysis, which the software selected as the scenes with the highest number of connections to other scenes.

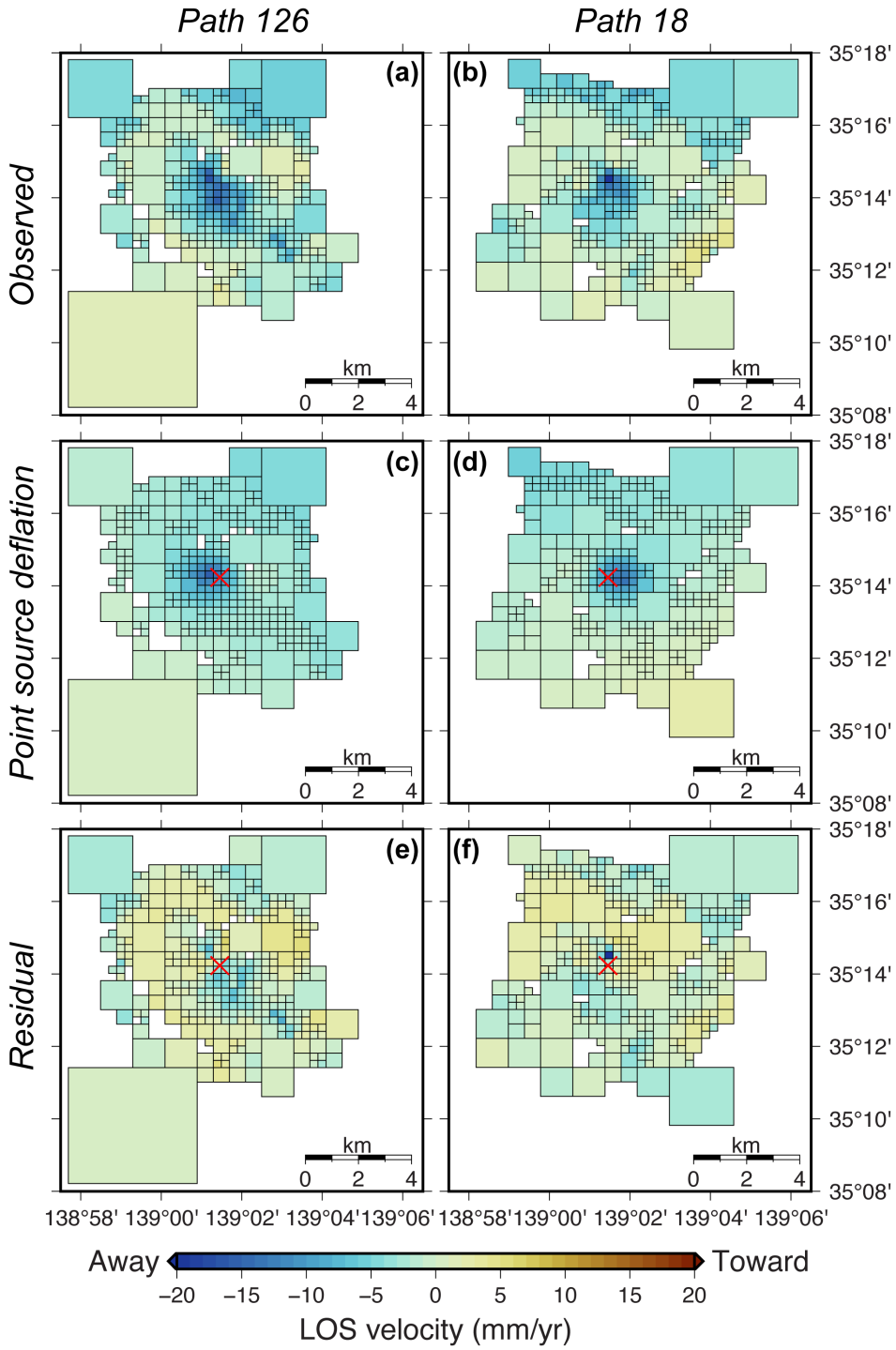

Figure S2. Results of inversion by the point source deflation model. Subsampled velocity datasets prepared by quadtree-partitioning for (a) path 126 and (b) path 18. Simulated velocities for (c) path 126 and (d) path 18, and residuals for (e) path 126 and (f) path 18. The red crosses indicate the locations of the estimated point source. The parameters and standard errors of the models are listed in Table 1.

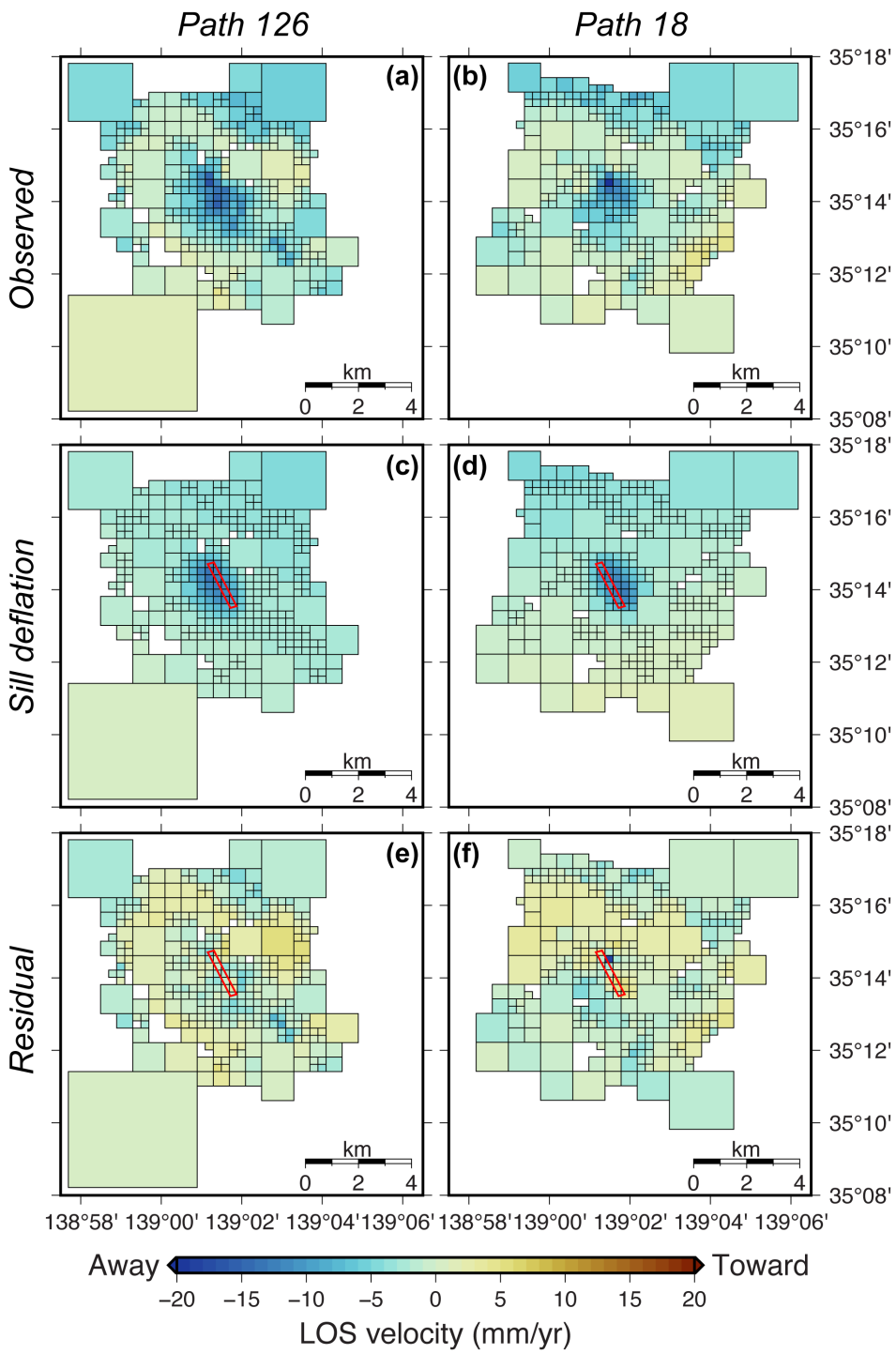

Figure S3. Results of inversion by the sill deflation model. Subsampled velocity datasets prepared by quadtree-partitioning for (a) path 126 and (b) path 18. Simulated velocities for (c) path 126 and (d) path 18, and residuals for (e) path 126 and (f) path 18. The red rectangles indicate the locations of the estimated sill model. The parameters and standard errors of the models are listed in Table 1.

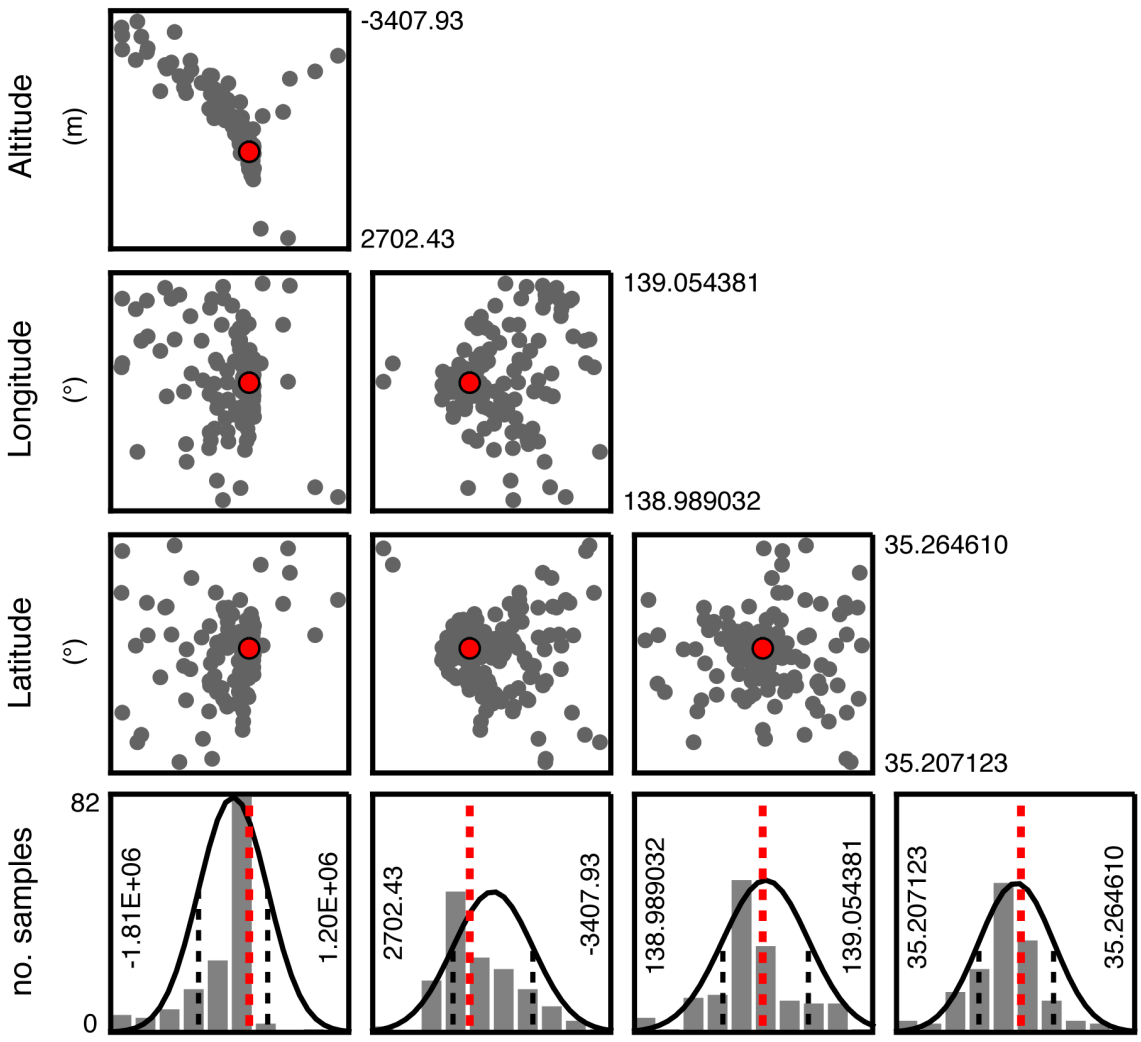

Figure S4. Standard deviation (histograms) and tradeoffs (scatter plots) between the model parameters for the point source deflation model. Red points and red dashed lines show the optimal parameters for the model.

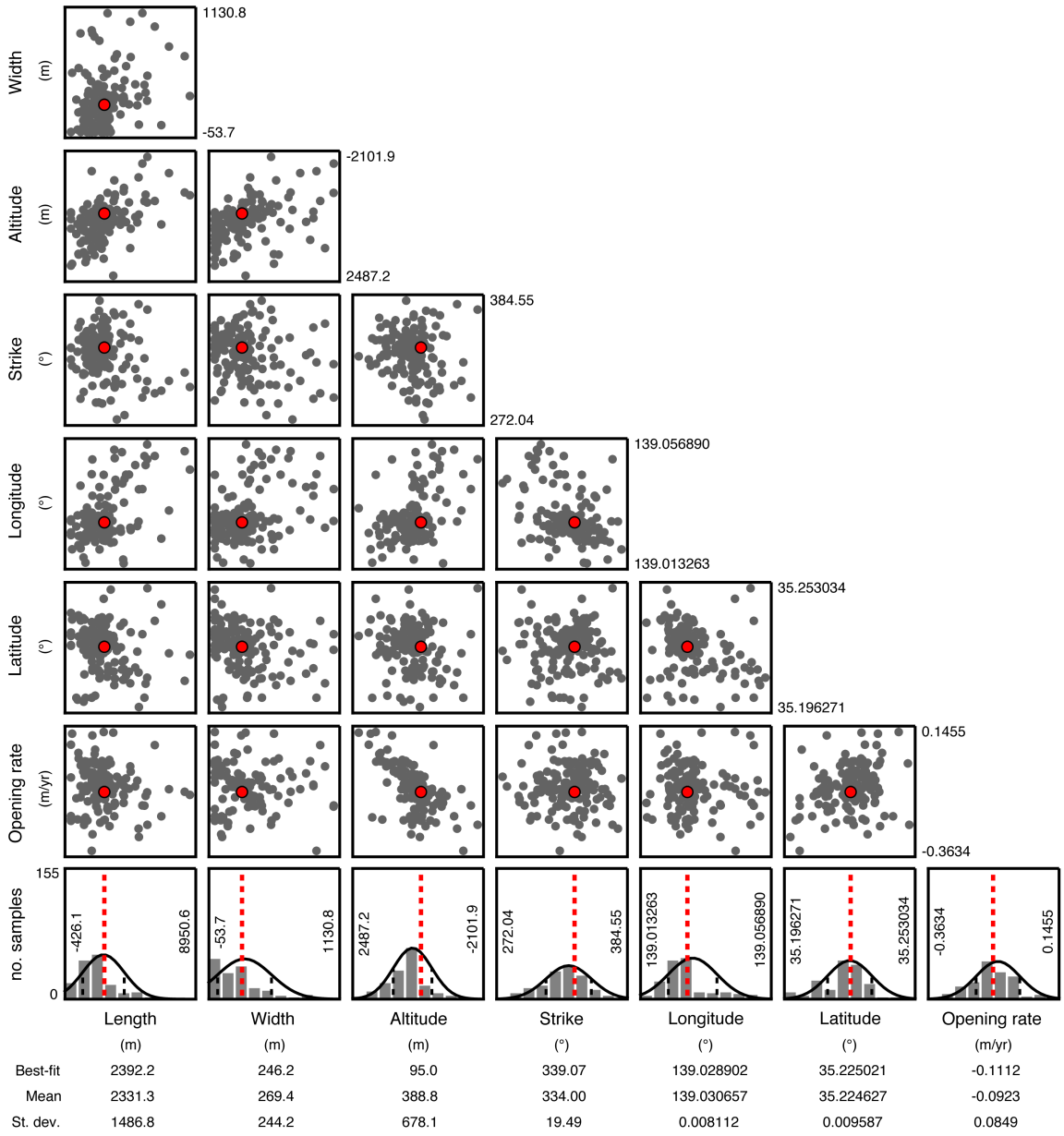

Figure S5. Standard deviation (histograms) and tradeoffs (scatter plots) between the model parameters for the sill deflation model. Red points and red dashed lines show the optimal parameters for the model.

Path 126 (Ascending, right-looking)		Path 18 (Descending, right-looking)	
Observation Date	Position [m] [a]	Observation Date	Position [m] [a]
10 July 2015	−84.0080	2 July 2015	−25.8004
24 July 2015	−234.737	16 July 2015	−246.664
1 April 2016	−24.5921	27 August 2015	−132.418
8 July 2016	−174.293	22 October 2015	−137.915
9 December 2016	−98.1012	14 January 2016	−75.3610
17 March 2017	−249.382	21 April 2016 [b]	0
23 June 2017	−205.337	14 July 2016	−167.343
13 April 2018	−154.725	22 September 2016	−172.853
15 March 2019	−264.493	15 December 2016	−300.976
21 June 2019	−277.087	6 April 2017	−68.6881
11 October 2019	−101.863	13 July 2017	−151.660
6 December 2019	−75.1073	21 September 2017	−322.930
3 January 2020	85.4325	14 December 2017	−180.590
17 January 2020	38.2575	5 April 2018	263.321
13 March 2020 [b]	0	12 July 2018	−25.3933
10 April 2020	−246.522	20 September 2018	−250.212
19 June 2020	−68.3064	13 December 2018	−206.409
4 December 2020	−64.6116	7 February 2019	148.452
18 December 2020	−113.811	4 April 2019	327.216
15 January 2021	−149.254	19 September 2019	−276.874
12 March 2021	−36.3006	12 December 2019	−458.007
		2 April 2020	74.0828
		17 September 2020	−196.891
		1 April 2021	268.010

[a] Positions are perpendicular baseline lengths between the scene and the super primary scene.

[b] The scenes used as the super primary scenes, which the software selected as the scenes with the highest number of connections to other scenes.

Table S1. ALOS-2/PALSAR-2 data used in this study.